

Lithium Deposition Induced Fracture of Carbon Nanotubules and Its Implication to Solid-State Batteries

Jingzhao Chen[†], Chao Zhao[§], Dingchuan Xue[†], Liqiang Zhang[†], Yongfu Tang^{†,‡}, Congcong Du[†], Tingting Yang[†], Xuedong Zhang[‡], Ruyue Fang^{†,‡}, Qinglong Chen[‡], Baiyu Guo[†], Hongjun Ye[†], Hui Li[†], Steve Harris[‡], Feng Ding^{§,}, Sulin Zhang^{†,*}, Jianyu Huang^{†,‡,*}.*

[†]Clean Nano Energy Center, State Key Laboratory of Metastable Materials Science and Technology, Yanshan University, Qinhuangdao 066004, P. R. China.

[§]Center for Multidimensional Carbon Materials, Institute for Basic Science (IBS), School of Materials Science and Engineering, Ulsan National Institute of Science and Technology (UNIST), Ulsan 44919, Republic of Korea.

[‡]Department of Engineering Science and Mechanics, The Pennsylvania State University, University Park, PA 16802, USA.

[‡]Hebei Key Laboratory of Applied Chemistry, College of Environmental and Chemical Engineering, Yanshan University, Qinhuangdao 066004, P.R. China.

[‡]Department of Material, The Pennsylvania State University, University Park, PA 16802, USA.

[‡]Energy Storage Division, Lawrence Berkeley, National Laboratory, Berkeley, CA 94720, USA.

[‡]School of Materials Science and Engineering, Xiangtan University, Xiangtan, Hunan 411105, P. R. China.

Corresponding Author

*Correspondence to: jyhuang8@hotmail.com; suzl0@psu.edu; f.ding@unist.ac.kr.

KEYWORDS: *Solid-state batteries, Li dendrite, Li propagation, Deposition stress and CNT fracture*

ABSTRACT: The increasing demand for safe and dense energy storage has shifted the research focus from organic liquid electrolyte-based Li-ion batteries toward solid-state batteries (SSBs). However, the application of SSBs is impeded by uncontrollable Li dendrite growth and short circuiting, mechanism of which remains elusive. Herein, we conceptualize a scheme to directly visualize Li deposition and propagation in submicron carbon nanotubes (CNTs) to mimic Li deposition dynamics in solid electrolytes (SEs), where the high-strength CNT walls mimic the mechanically strong SEs. We observed that the deposited Li propagates as a creeping solid in the CNTs, presenting an effective pathway for stress relaxation. When the stress-relaxation pathway is blocked, Li deposition induced stress causes CNT fracture. Our mechanics analysis suggests that interfacial lithiophilicity critically governs Li deposition dynamics and stress relaxation. Our study offers critical strategies for suppressing Li dendritic growth and constructing high energy density, electrochemically and mechanically robust SSBs.

■ INTRODUCTION

Vehicle electrification and grid energy storage demand for energy storage technologies with much higher energy densities than the existing technologies.^{1, 2} Lithium (Li) metal solid-state battery (SSB) has emerged as one of the most attractive energy storage technologies for its high energy density and improved safety due to the use of the high-capacity Li-metal anode and ceramic solid electrolytes (SEs).³⁻⁵ However, Li metal deposition requires free volume around the deposition sites and may otherwise generate large mechanical stress, which can be transmitted to the surrounding solid components, leading to fracture of the components, including SEs. The fracture surfaces further attract Li metal propagation and penetration into the SEs, causing uncontrollable Li dendrite growth and short circuiting^{2, 6, 7}. To elucidate the Li dendrite growth mechanisms under the complex electrochemomechanical environment, significant progress has been made to imaging the dendrite growth in SEs by in-situ optical microscopy.⁸⁻¹⁰ In contrast, in-situ transmission electron microscopy (TEM) visualization of the dendrite nucleation and propagation in solid media remains very challenging as such processes are deeply buried within the SSBs.^{11, 12} As a result, a mechanistic understanding of the Li dendrite growth in SSBs is still lacking.^{8, 13-17}

We here conceptualize a scheme to directly visualize Li deposition and propagation in a sub-micron carbon nanotube (CNT) inside an environmental transmission electron microscope (ETEM), whereby the high-strength CNT mimics the mechanically strong SEs that confine Li deposition and growth. We reveal that interfacial lithiophilicity critically mediates Li dendrite growth dynamics and mechanical stress relaxation and accumulation in the CNT. Once the stress relaxation pathway is blocked, a very large stress can be generated and transmitted to the CNT, causing CNT fracture. Our results thus suggest that Li deposition induced stress can be similarly high enough to cause crack nucleation and propagation in SEs.

■ RESULTS AND DISCUSSION

Li deposition was achieved in an electrochemical device comprising a Li metal anode, a naturally formed Li_2CO_3 layer as the SE and a hollow CNT as the counter electrode operating in a CO_2 ambient in an aberration-corrected ETM.^{11, 18-20} The initial CNT has an outer diameter of 361 nm and an inner diameter of 306 nm with a wall thickness of 27.5 nm (Figure S1a). When a

negative potential was applied to the CNT, the CNT wall was first lithiated (Figure S1b), resulting in an increase of the wall thickness from the initial 27.5 nm to 51 nm after 430 s lithiation. Selected area electron diffraction (SAED, Figure S1c, d) and electron energy loss spectroscopy (EELS, Figure S1e, f) confirm the lithiation of the CNT. High-resolution transmission electron microscopy (HRTEM) indicates the amorphous and turbostratic nature of the pristine CNT wall (Figure S1g) and the presence of Li_2CO_3 after lithiation (Figure S1h). Further lithiation leads to Li deposition in the hollow of the CNT. Lithiation of the CNT can also be performed from the radial direction of the CNT (Figure S2 and Supplementary Movie S1). We found that the thickness of the CNT walls increased 120.9% on average (Figure S3), corresponding to a volume expansion of 114.9%, which is much larger than that of lithiated graphite. For a well graphitized CNT, assuming lithiation to LiC_6 , the volume expansion is estimated to be 10%.²¹ The large volume expansion in amorphous CNT implies other Li storage mechanisms than intercalation are operating.²² Noticeably, the lithiated CNT is a mixed ionic-electronic conductor (MIEC), which is both mechanically robust and electrochemically stable against the corrosive Li metal. Such a MIEC can be used as an ideal host of Li metal to construct three-dimensional (3D) SSBs. Therefore, in addition to explore Li deposition induced mechanical instability of SEs, our study provides a direct demonstration of a MIEC-enabled Li metal host for Li metal anodes.¹¹

During the Li deposition process, we observed frequent fracture of CNTs, with two sets of experimental results shown in Figure 1. In Figure 1a-i the deposition initiated from the middle of the CNT where a nanoparticle (determined to be Al_2O_3 , Figure S4) was present (Figure 1a-b and Supplementary Movie S2). The Al_2O_3 nanoparticle appeared to be a nucleation site for Li deposition. The Li metal grew in length towards the two ends of the lithiated CNT (Figure 1c-d), and the length with time exhibits a linear relationship (Figure S5), suggesting a reaction-controlled growth process. Interestingly, our in-situ experiments evidenced symmetry breaking of the growing fronts of the Li metal inside the CNT. Both fronts propagated forward at the beginning of Li deposition. The front far from the SE (hereafter denoted as the far front) arrested after a certain period of Li deposition, while the front near the SE (the near front) continued to propagate until it reached the SE at 203 s. Further Li deposition was fully constrained by the SE, the far front, and the CNT. At 217 s a bump emerged on the left wall of the CNT (Figure 1e, white arrow), which then grew (Figure 1f) until fracture of the CNT wall occurred on the left wall of the CNT (Figure 1g, h). Evidently, the stress relaxation due to the cracking altered Li-metal growth pathway from

longitudinal to the radial direction along the crack. At 367 s the crack appeared to have propagated to the right side of the CNT wall (Figure 1i, white arrow on the right), and the growth then proceeded radially along the crack. It should be noted that the fronts of Li in the CNT were covered by a thin layer of Li_2CO_3 ^{23,24} (Figure 1I-III), which may exert a back pressure against the growing Li and cause stress buildup in the deposited Li. Figure 1j-p (Supplementary Movie S3) is another experiment showing fracture of a CNT after 3068 s of Li deposition. Again the deposition changed its course once fracture occurred in the CNT (Figure 1p). More Li deposition induced fracture of CNTs is depicted in Figure S6 (Supplementary Movies S4 and S5), which demonstrates similar behavior to that shown in Figure 1.

We carried out parallel in-situ TEM experiments in vacuum condition and observed distinctly different phenomena. In vacuum, the symmetry breaking of the Li front propagation was nearly absent, as both the near and far fronts propagated continuously until the CNT was fully filled with Li metal. Corresponding to the less predominant symmetry breaking of Li metal front propagation, cracking of the CNTs in vacuum was not observed (Figure S7 and Supplementary Movie S6).

The Li deposition induced fracture of CNT is surprising, as the fracture strength of CNT is considered very high.²⁵ Because the structure of the CNT in our experiments consists of mainly disordered or near amorphous carbon, its mechanical strength differs considerably from that of well-graphitized arc discharged CNTs. Therefore, we conducted both tensile (along the longitudinal direction) and compression experiments (along the radial direction) on the pristine and lithiated CNTs using either a home-made ETEM-AFM (atomic force microscopy) platform^{24,26} or a Hysitron PI 95 TEM sample holder. Corresponding schematics of ETEM-AFM used for the compression from the radial direction or the tensile from the longitudinal direction of the pristine/lithiated CNTs are depicted in Figure S8a and c, respectively (Figure S8b, d shows the TEM images of the compression and tensile tests, respectively). Figure 2 shows tensile tests conducted on both the pristine (Figure 2a-h and Supplementary Movie S7) and lithiated CNTs (Figure 2j-q and Supplementary Movie S8). Both the pristine and lithiated CNTs exhibit brittle fracture with sharp fractured surfaces perpendicular to the longitudinal direction of the CNTs (Figure 2h, q). The fracture strengths of the pristine and the lithiated CNTs were measured to be 1.45 GPa and 0.93 GPa, respectively. Apparently, the mechanical strength of the lithiated CNT is weaker than that of the pristine CNT. More tensile tests of both the pristine and lithiated CNTs are

shown in Figure S9 (Supplementary Movies S9 and S10), and the results are consistent with that shown in Figure 2.

As lithiation-induced fracture occurred along the hoop direction, we speculate that the fracture strength along the hoop direction of the CNT may be more relevant to the lithiation-induced fracture event. Therefore, we conducted compression experiments along the radial direction for both the pristine (Figure 3a-f and Supplementary Movie S11) and lithiated (Figure 3g-l and Supplementary Movie S12) CNTs. The pristine CNT is highly elastic: it was almost flattened after compression (Figure 3e) yet it recovered to its original shape after release from the compression (Figure 3f), and the process is highly repeatable. After even 4 cycles of repeated flattening, it still recovered to its initial shape, indicating high elasticity of the amorphous CNT (Figure S10 and Supplementary Movie S11). Although the CNT recovered to its tubular structure after every compression (Figures 3a-f and S10), the corresponding force-displacement curves (Figure 3p) shows that the maximum attainable force dropped significantly after the 1st compression experiments, suggesting that some carbon-carbon bonds in the amorphous CNT may have been damaged after the 1st compression. However, the force-displacement curves (Figure 3p) were repeatable after the 1st compression, suggesting that most damages to the CNT structure occurred in the first compression. More experimental tests are shown in Figures S10 and S11a-f (Supplementary Movies S11 and S13), showing the repeatability of these experimental tests.

In contrast to the pristine CNT, the lithiated CNT exhibit less elasticity. In fact, it fractured after the 1st compression experiment (Figures 3g-l, S11g-l and S12, Supplementary Movies S12 and S14), suggesting lithiation induced embrittlement of the CNT, which is consistent with our previous studies of lithiation induced embrittlement of CNTs.²⁷ To correlate the radial compressive loading in the experiments with the stress state in the CNT, we invoked finite element analyses (FEA) to quantify the stress states using the package Abaqus.^{28, 29}

The simulated force-displacement plot (Figure 3p, purple curve) reproduces the experimental measurements very well. The maximum hoop and axial stress versus displacement curves of the pristine CNTs are shown in Figure 3p (red and blue curves), where an inflection point of the curve (marked by a red arrow) indicates a transition of the maximum hoop stress from the center of inner CNT wall to both edges of the flattened CNT wall. Such a transition can be clearly seen in the stress distributions shown in Figure 3m-o. According to the FEA analysis, the maximum hoop and

axial stress of the pristine CNTs was estimated to be 1.36 and 1.2 GPa, respectively. The stress versus displacement curves of the lithiated CNTs are shown in [Figure 3t](#) and the hoop stress distributions during the compression are shown in [Figure 3q-s](#), from which we can see that both the simulated deformation of the lithiated CNT and the force-displacement curve agree with the experimental measurements very well. The critical maximum hoop stress of the lithiated CNTs is estimated to be 1.84 GPa which is greater than the critical maximum axial stress of 1.35 GPa, implying that the fracture should occur along the hoop direction. More in-situ compression experiments and FEA simulations are shown in [Figure S11](#). From FEA we estimate that critical maximum hoop and axial stress of the pristine CNT is 1.8 and 1.1 GPa, respectively, and the breaking strength of the lithiated CNTs is 2.0 ~ 2.53 GPa if the maximum hoop stress is considered. The maximum equivalent stresses of the pristine and lithiated CNTs are presented in [Figures S13](#) and [S14](#).

In a tensile test, a CNT failure always starts from the weakest point of the CNT wall and thus tensile test generally results in a low strength due to defects in CNT. In contrast, the indentation test breaks a CNT from a local point, whose strength could be much higher than that measured by tensile test. The maximum pressure inside the CNT is estimated to be from 247 to 1000 MPa ([Supplementary Section 5, Figures S13 and S14](#)).

To further appreciate the correlations between the symmetry breaking of the moving fronts and the fracture of CNT, we below analyze Li deposition dynamics and stress generation and transmission in the constituent materials during Li deposition. As Li deposition is limited by the diffusion of Li ions, Li deposition, once nucleated, likely occurs in the proximity of the near front of Li. Li deposition in this region generates volumetric chemical strain and compressive stress, denoted by σ_0 . The compressive stress is then transmitted to the Li fronts as well as the CNT, driving the propagation of Li fronts and fracture of CNT, respectively.

The transmission of the compressive stress to the surrounding components depends on the materials properties of Li and the Li/CNT interface. Li is soft with a homologous temperature of 0.66 and exhibits creeping behavior.³⁰⁻³² In vacuum, residual oxygens react with Li, forming a thin Li₂O layer. The Li₂O layer is relatively lithiophilic, with a wetting angle of ~90° at the interface ([Figure S15a](#)). Thus Li flows along the CNT with little interfacial resistance. In CO₂ environment, on the other hand, a thin layer of Li₂CO₃ is formed at the interface.^{23, 24} The Li₂CO₃ layer is less

lithiophilic than the Li_2O layer, as indicated by a much larger wetting angle ($\sim 126^\circ$) at the interface (Figure S15b-e). Thus, considerable shear resistance is generated at the interface. Here, we assume that the interfacial shear stress τ is proportional to the radial stress σ_r of Li near the interface: $\tau = \mu\sigma_r$, where μ is interfacial friction coefficient that measures the lithiophilicity of the interfaces. Assuming Li metal is nearly incompressible, the stress state in the Li metal is approximately hydrostatic, denoted by σ_m . Treating the shear stress as a body force that is uniformly distributed in Li, mechanics balance yields the hydrostatic stress along the axial (z) direction:

$$\sigma_m = \sigma_0 e^{-\frac{2\mu}{R}z} \quad (1)$$

where R is the radius of the CNT. Equation (1) shows that the hydrostatic stress in Li metal exponentially decays from the near front to the far front, with a decay constant $\frac{2\mu}{R}$. For a very weak interfacial shear resistance as in vacuum condition, $\mu \sim 0$, Li encased in the CNT acts as an incompressible fluid that uniformly transmits the deposition stress σ_0 from the deposition site to all the surrounding materials with negligible decay (Figure 4b). The entire Li whisker experiences the same level of hydrostatic compressive stress σ_0 . Thus, the near and far fronts undergo the same propelling force and both propagate to lengthen Li. The propagation of both the Li metal fronts causes instantaneous stress relaxation, giving rise to a low stress level σ_0 . Accordingly, the stresses transmitted to the CNT is insufficient to cause fracture. On the other hand, in CO_2 environment, the appreciable shear resistance causes decays in the stresses (Figure 4c). The near and far fronts thus undergo uneven propelling forces, breaking the symmetry: the near front continues to propagate while the far front arrests. Stress relaxation in CO_2 environment relies solely on the near front propagation. Once the near front reaches the SE, stress relaxation becomes impeded, Li deposition switches to a root growth mode and the deposition stress rapidly arises,³³ causing fracture of the CNT.

To determine the critical deposition stress σ_0 to cause CNT fracture, a simple mechanics analysis shows that the hoop direction of the CNT ($\sigma_{\text{CNT,H}}$) experiences a stress twice as much as in the axial direction ($\sigma_{\text{CNT,A}}$), suggesting that fracture would likely occur in the hoop direction of the CNT. Specifically, the hydrostatic stress in the Li metal is transmitted to CNT by: $\sigma_{\text{CNT,H}} = \frac{R}{\delta_{\text{CNT}}} \sigma_m$, where $\frac{R}{\delta_{\text{CNT}}}$ is a geometric amplification factor of the stress and δ_{CNT} are the thicknesses of the CNT. Given $R \sim 160$ nm and $\delta_{\text{CNT}} \sim 20$ nm, the geometric factor is roughly 8 fold for the CNTs.

Assuming that the friction coefficient $\mu \sim 0.1$, and since the fracture site is about $\sim 10R$ from the SE (Figure 2), the deposition stress decays by a few folds: $\sigma_m \sim \sigma_0/3$. The stress transmitted to the CNT at the fracture site is $8 \times \sigma_0/3$. Considering that the fracture strength of the lithiated CNT is ~ 1.0 GPa, the deposition stress accumulated in Li metal is $\sigma_0 \sim 375$ MPa in order to fracture the CNT, corresponding to an applied overpotential of ~ 50 mV. Clearly, the deposition stress, which is compressive, is transmitted to a very large tensile stress in CNT, causing CNT fracture in our experiments. Such a compression-to-tension conversion may also occur in SEs, depending on the geometry of the surrounding components. The high level of deposition stress, if built up in SEs, may likely cause the fracture of SEs at the defected sites.

■ CONCLUSIONS

In summary, we used CNTs to mimic SEs and carried out in-situ TEM studies on the Li deposition induced fracture of the CNTs. Our accompanying mechanics analysis reveals that stress relaxation plays a critical role to maintain the structural stability of the solid components during Li deposition. For a lithiophilic Li/CNT interface, Li flows along the CNT with little shear resistance, and the deposition induced stress is fast relaxed. When such stress relaxation pathways are blocked, Li deposition induced stress can be very high on the GPa level, causing fracture of the lithiated CNTs. Extending these findings to SEs and given the high rigidity and low fracture strength of typical SEs such as LLZO, Li deposition may generate similarly high stress to fracture the SEs, which may subsequently trigger short circuiting. Our results suggest that the electrochemomechanical stability of high-energy density SSBs hinges upon the interfacial engineering to facilitate stress relaxation, reduce the interfacial impedance thus the overpotential, and minimize the flaw size thus increasing the fracture strength of SEs. In addition, as MIEC represents an important class of 3D Li metal hosts, our results also have important implications in constructing Li-metal anodes with a 3D porous architecture for simultaneously maintaining mechanical and electrochemical stability of the SSBs.

■ ASSOCIATED CONTENT

Supporting Information

The authors declare that all data supporting the findings of this study is available within the Article and its Supplementary Information files. Any other data will be provided by the corresponding author upon request.

■ AUTHOR INFORMATION

Corresponding Authors

E-mail: jyhuang8@hotmail.com; suz10@psu.edu; f.ding@unist.ac.kr.

Author Contributions

Liqiang Zhang, Yongfu Tang and Jianyu Huang conceived and designed the project. Xuedong Zhang and Hongjun Ye fabricated the samples. Jingzhao Chen, Baiyu Guo and Congcong Du carried out the *in-situ* ETEM experiments. Liqiang Zhang, Yongfu Tang and Jianyu Huang supervised the experiments. Feng Ding, Sulin Zhang and Jianyu Huang co-wrote the paper. Jingzhao Chen, Chao Zhao and Dingchuan Xue contribute equally to this work. All the authors discussed the results and commented on the manuscript.

Notes

The authors declare no competing financial interest.

■ ACKNOWLEDGMENTS

This work was financially supported by the National Natural Science Foundation of China (Nos. 52022088, 51971245, 51772262, 21406191, U20A20336, 21935009), Beijing Natural Science Foundation (2202046), Fok Ying-Tong Education Foundation of China (No. 171064), Natural Science Foundation of Hebei Province (No. B2020203037, B2018203297), Hunan Innovation Team (2018RS3091), Institute for Basic Science (IBS-R019-D1) of South Korea. Part of this work was supported by the Assistant Secretary for Energy, Vehicles Technology Office, of the U.S. Department of Energy under Contract (No. DEAC02-05CH11231).

■ REFERENCES

- (1) Lewis, N. S. Powering the Planet. *MRS Bull.* **2007**, *32*,808-820.
- (2) Tang, Y.; Zhang, L.; Chen, J.; Sun, H.; Yang, T.; Liu, Q.; Huang, Q.; Zhu, T.; Huang, J. Electro-chemo-mechanics of lithium in solid state lithium metal batteries. *Energy Environ. Sci.* **2021**, *14*,602-642.
- (3) Xu, S.; McOwen, D. W.; Wang, C.; Zhang, L.; Luo, W.; Chen, C.; Li, Y.; Gong, Y.; Dai, J.; Kuang, Y.; Yang, C.; Hamann, T. R.; Wachsman, E. D.; Hu, L. Three-Dimensional, Solid-State Mixed Electron-Ion Conductive Framework for Lithium Metal Anode. *Nano Letters* **2018**, *18*,3926-3933.
- (4) Dong, D.; Zhou, B.; Sun, Y.; Zhang, H.; Zhong, G.; Dong, Q.; Fu, F.; Qian, H.; Lin, Z.; Lu, D.; Shen, Y.; Wu, J.; Chen, L.; Chen, H. Polymer Electrolyte Glue: A Universal Interfacial Modification Strategy for All-Solid-State Li Batteries. *Nano Letters* **2019**, *19*,2343-2349.
- (5) Zhou, J.; Qian, T.; Liu, J.; Wang, M.; Zhang, L.; Yan, C. High-Safety All-Solid-State Lithium-Metal Battery with High-Ionic-Conductivity Thermoresponsive Solid Polymer Electrolyte. *Nano Letters* **2019**, *19*,3066-3073.
- (6) Song, Y.; Yang, L.; Zhao, W.; Wang, Z.; Zhao, Y.; Wang, Z.; Zhao, Q.; Liu, H.; Pan, F. Revealing the Short-Circuiting Mechanism of Garnet-Based Solid-State Electrolyte. *Adv. Energy Mater.* **2019**, *9*,1900671.
- (7) Kasemchainan, J.; Zekoll, S.; Spencer Jolly, D.; Ning, Z.; Hartley, G. O.; Marrow, J.; Bruce, P. G. Critical stripping current leads to dendrite formation on plating in lithium anode solid electrolyte cells. *Nat. Mater.* **2019**, *18*,1105-1111.
- (8) Kazyak, E.; Garcia-Mendez, R.; LePage, W. S.; Sharafi, A.; Davis, A. L.; Sanchez, A. J.; Chen, K.-H.; Haslam, C.; Sakamoto, J.; Dasgupta, N. P. Li Penetration in Ceramic Solid Electrolytes: Operando Microscopy Analysis of Morphology, Propagation, and Reversibility. *Matter* **2020**, *2*,1025-1048.
- (9) Sanchez, A. J.; Kazyak, E.; Chen, Y.; Chen, K.-H.; Pattison, E. R.; Dasgupta, N. P. Plan-View Operando Video Microscopy of Li Metal Anodes: Identifying the Coupled Relationships among Nucleation, Morphology, and Reversibility. *ACS Energy Lett* **2020**, *5*,994-1004.
- (10) Krauskopf, T.; Dippel, R.; Hartmann, H.; Peppler, K.; Mogwitz, B.; Richter, F. H.; Zeier, W. G.; Janek, J. Lithium-Metal Growth Kinetics on LLZO Garnet-Type Solid Electrolytes. *Joule* **2019**, *3*,2030-2049.

- (11) Chen, Y.; Wang, Z.; Li, X.; Yao, X.; Wang, C.; Li, Y.; Xue, W.; Yu, D.; Kim, S. Y.; Yang, F.; Kushima, A.; Zhang, G.; Huang, H.; Wu, N.; Mai, Y.-W.; Goodenough, J. B.; Li, J. Li metal deposition and stripping in a solid-state battery via Coble creep. *Nature* **2020**, *578*,251-255.
- (12) Deng, Z.; Lin, X.; Huang, Z.; Meng, J.; Zhong, Y.; Ma, G.; Zhou, Y.; Shen, Y.; Ding, H.; Huang, Y. Recent Progress on Advanced Imaging Techniques for Lithium-Ion Batteries. *Adv. Energy Mater.* **2021**, *11*,2000806.
- (13) Porz, L.; Swamy, T.; Sheldon, B. W.; Rettenwander, D.; Frömling, T.; Thaman, H. L.; Berendts, S.; Uecker, R.; Carter, W. C.; Chiang, Y.-M. Mechanism of Lithium Metal Penetration through Inorganic Solid Electrolytes. *Adv. Energy Mater.* **2017**, *7*,1701003.
- (14) Shishvan, S. S.; Fleck, N. A.; McMeeking, R. M.; Deshpande, V. S. Growth rate of lithium filaments in ceramic electrolytes. *Acta Mater.* **2020**, *196*,444-455.
- (15) Shishvan, S. S.; Fleck, N. A.; McMeeking, R. M.; Deshpande, V. S. Dendrites as climbing dislocations in ceramic electrolytes: Initiation of growth. *J. Power Sources* **2020**, *456*,227989.
- (16) Han, F.; Westover, A. S.; Yue, J.; Fan, X.; Wang, F.; Chi, M.; Leonard, D. N.; Dudney, N. J.; Wang, H.; Wang, C. High electronic conductivity as the origin of lithium dendrite formation within solid electrolytes. *Nat. Energy* **2019**, *4*,187-196.
- (17) Qi, Y.; Ban, C.; Harris, S. J. A New General Paradigm for Understanding and Preventing Li Metal Penetration through Solid Electrolytes. *Joule* **2020**, *4*,2599-2608.
- (18) Liu, X. H.; Zheng, H.; Zhong, L.; Huang, S.; Karki, K.; Zhang, L. Q.; Liu, Y.; Kushima, A.; Liang, W. T.; Wang, J. W.; Cho, J.-H.; Epstein, E.; Dayeh, S. A.; Picraux, S. T.; Zhu, T.; Li, J.; Sullivan, J. P.; Cumings, J.; Wang, C.; Mao, S. X.; Ye, Z. Z.; Zhang, S.; Huang, J. Y. Anisotropic Swelling and Fracture of Silicon Nanowires during Lithiation. *Nano Letters* **2011**, *11*,3312-3318.
- (19) Liu, X. H.; Huang, J. Y. In situ TEM electrochemistry of anode materials in lithium ion batteries. *Energy Environ. Sci.* **2011**, *4*,3844-3860.
- (20) Liu, X. H.; Liu, Y.; Kushima, A.; Zhang, S.; Zhu, T.; Li, J.; Huang, J. Y. In Situ TEM Experiments of Electrochemical Lithiation and Delithiation of Individual Nanostructures. *Adv. Energy Mater.* **2012**, *2*,722-741.
- (21) Sato, K.; Noguchi, M.; Demachi, A.; Oki, N.; Endo, M. A Mechanism of Lithium Storage in Disordered Carbons. *Science* **1994**, *264*,556-558.
- (22) Liu, Y.; Xue, J. S.; Zheng, T.; Dahn, J. R. Mechanism of lithium insertion in hard carbons prepared by pyrolysis of epoxy resins. *Carbon* **1996**, *34*,193-200.

- (23) Yang, T.; Jia, P.; Liu, Q.; Zhang, L.; Du, C.; Chen, J.; Ye, H.; Li, X.; Li, Y.; Shen, T.; Tang, Y.; Huang, J. Air-Stable Lithium Spheres Produced by Electrochemical Plating. *Angew. Chem., Int. Ed.* **2018**, *57*, 12750-12753.
- (24) Zhang, L.; Yang, T.; Du, C.; Liu, Q.; Tang, Y.; Zhao, J.; Wang, B.; Chen, T.; Sun, Y.; Jia, P.; Li, H.; Geng, L.; Chen, J.; Ye, H.; Wang, Z.; Li, Y.; Sun, H.; Li, X.; Dai, Q.; Tang, Y.; Peng, Q.; Shen, T.; Zhang, S.; Zhu, T.; Huang, J. Lithium whisker growth and stress generation in an in situ atomic force microscope–environmental transmission electron microscope set-up. *Nat. Nanotechnol.* **2020**, *15*, 94-98.
- (25) Li, L.; Lindquist, S. Creating a Protein-Based Element of Inheritance. *Science* **2000**, *287*, 661-664.
- (26) Liu, Q.; Zhang, L.; Sun, H.; Geng, L.; Li, Y.; Tang, Y.; Jia, P.; Wang, Z.; Dai, Q.; Shen, T.; Tang, Y.; Zhu, T.; Huang, J. In Situ Observation of Sodium Dendrite Growth and Concurrent Mechanical Property Measurements Using an Environmental Transmission Electron Microscopy–Atomic Force Microscopy (ETEM-AFM) Platform. *ACS Energy Lett* **2020**, *5*, 2546-2559.
- (27) Liu, Y.; Zheng, H.; Liu, X. H.; Huang, S.; Zhu, T.; Wang, J.; Kushima, A.; Hudak, N. S.; Huang, X.; Zhang, S.; Mao, S. X.; Qian, X.; Li, J.; Huang, J. Y. Lithiation-Induced Embrittlement of Multiwalled Carbon Nanotubes. *ACS Nano* **2011**, *5*, 7245-7253.
- (28) Yang, W.; Yang, J.; Dong, Y.; Mao, S.; Gao, Z.; Yue, Z.; Dillon, S. J.; Xu, H.; Xu, B. Probing buckling and post-buckling deformation of hollow amorphous carbon nanospheres: In-situ experiment and theoretical analysis. *Carbon* **2018**, *137*, 411-418.
- (29) Yang, W.; Mao, S.; Yang, J.; Shang, T.; Song, H.; Mabon, J.; Swiech, W.; Vance, J. R.; Yue, Z.; Dillon, S. J.; Xu, H.; Xu, B. Large-deformation and high-strength amorphous porous carbon nanospheres. *Sci. Rep.* **2016**, *6*, 24187.
- (30) Masias, A.; Felten, N.; Garcia-Mendez, R.; Wolfenstine, J.; Sakamoto, J. Elastic, plastic, and creep mechanical properties of lithium metal. *J. Mater. Sci.* **2019**, *54*, 2585-2600.
- (31) Wang, Z.; Li, X.; Chen, Y.; Pei, K.; Mai, Y.-W.; Zhang, S.; Li, J. Creep-Enabled 3D Solid-State Lithium-Metal Battery. *Chem* **2020**, *6*, 2878-2892.
- (32) Masias, A.; Felten, N.; Sakamoto, J. Characterizing the mechanical behavior of lithium in compression. *J. Mater. Res.* **2021**, *36*, 729-739.

(33) Kushima, A.; So, K. P.; Su, C.; Bai, P.; Kuriyama, N.; Maebashi, T.; Fujiwara, Y.; Bazant, M. Z.; Li, J. Liquid cell transmission electron microscopy observation of lithium metal growth and dissolution: Root growth, dead lithium and lithium flotsams. *Nano Energy* **2017**, *32*, 271-279.

Figures

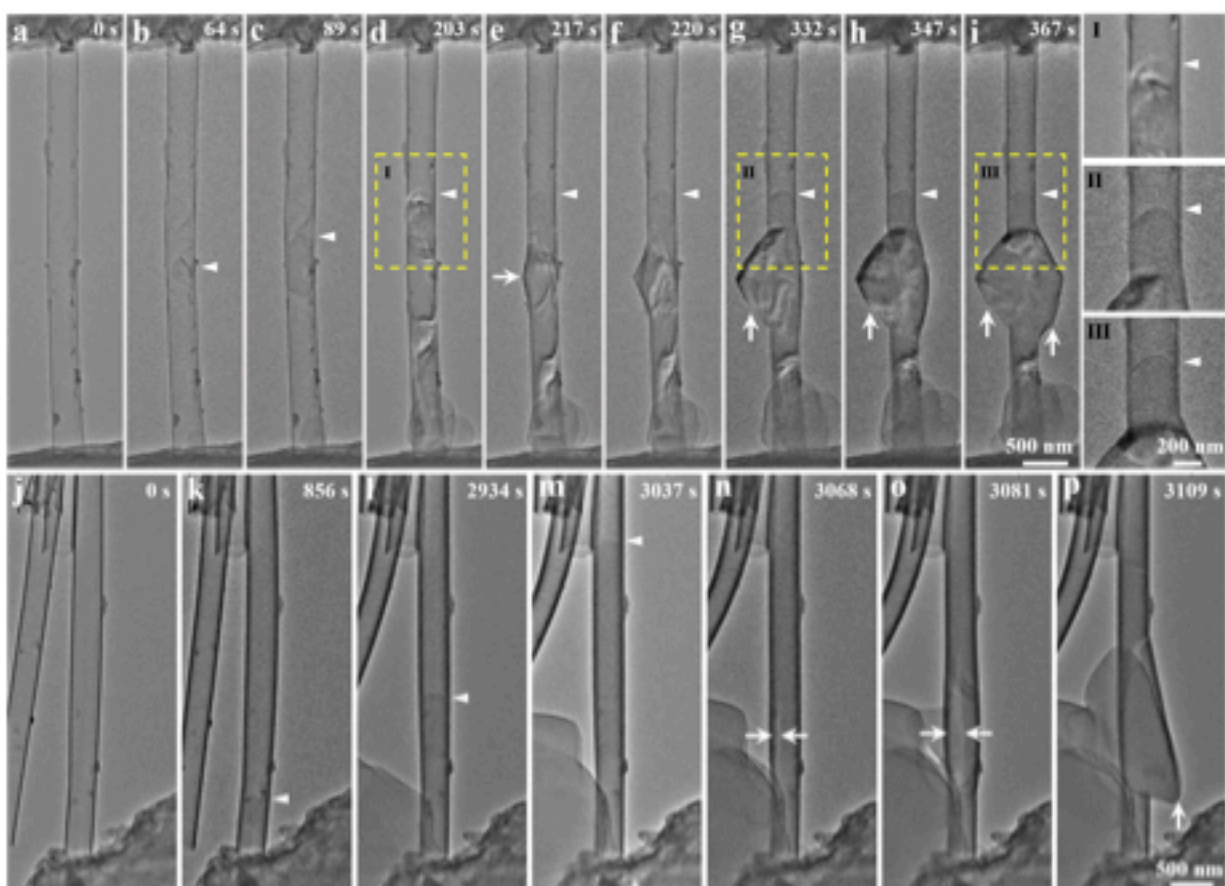


Figure 1. Two sets of time lapse TEM images (a-i, j-p) showing the fracture of CNTs induced by lithium deposition in a CO_2 ambient. The applied voltage was -0.8 V in (a-i) and -1 V in (j-p). "I" to "III" are local magnification of "(d)", "(g)" and "(i)", respectively, showing the front of the deposited lithium was covered with a thin layer of Li_2CO_3 . Arrowheads point out the lithium deposition fronts. White arrows point out the fracture location of the CNT walls.

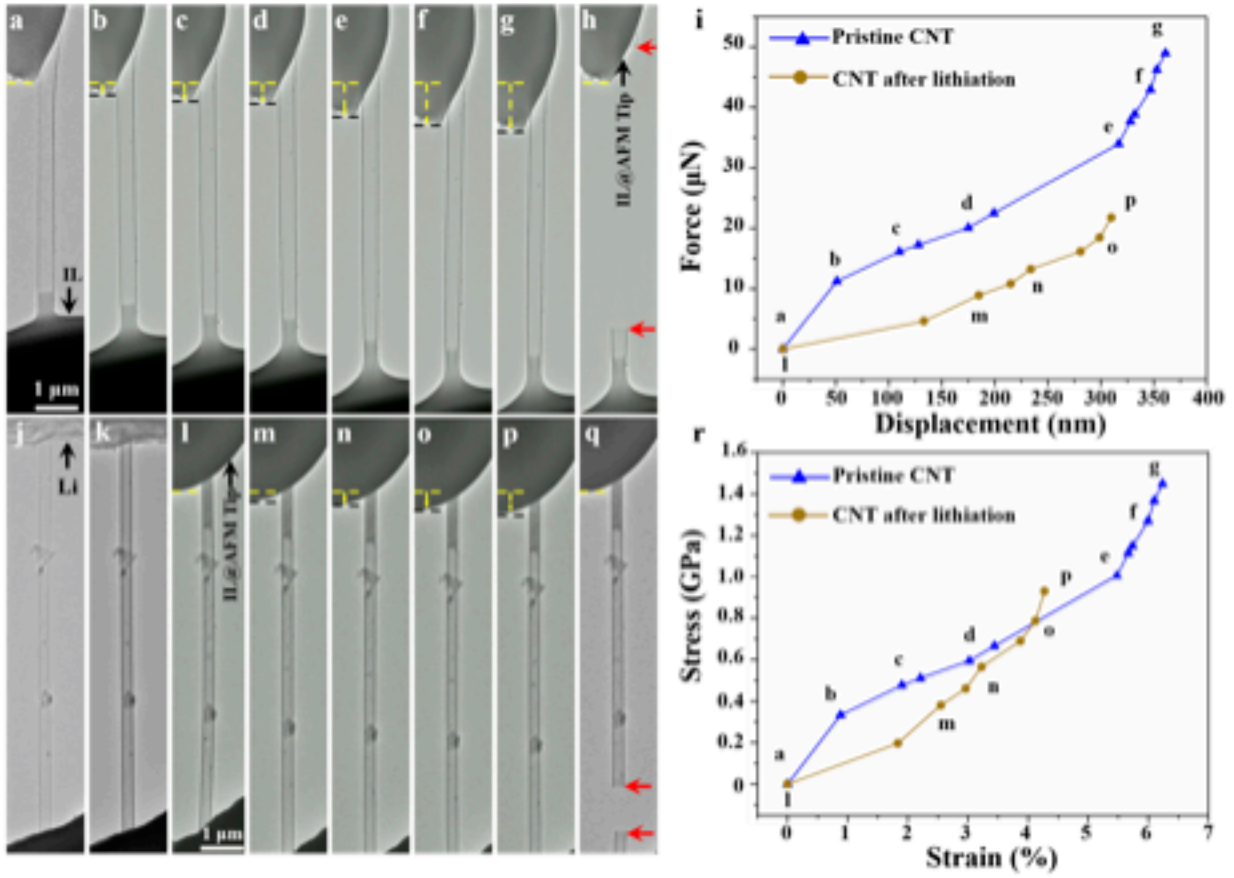


Figure 2. Tensile experiments in the pristine (a-h) and lithiated (j-q) CNTs. Both the pristine and the lithiated CNTs exhibit brittle fracture showing a sharp fracture surface (red arrows) perpendicular to the longitudinal direction of the CNT (h, q). (i) and (r) are force-displacement and stress-strain plots corresponding to (a-h) and (l-q), respectively.

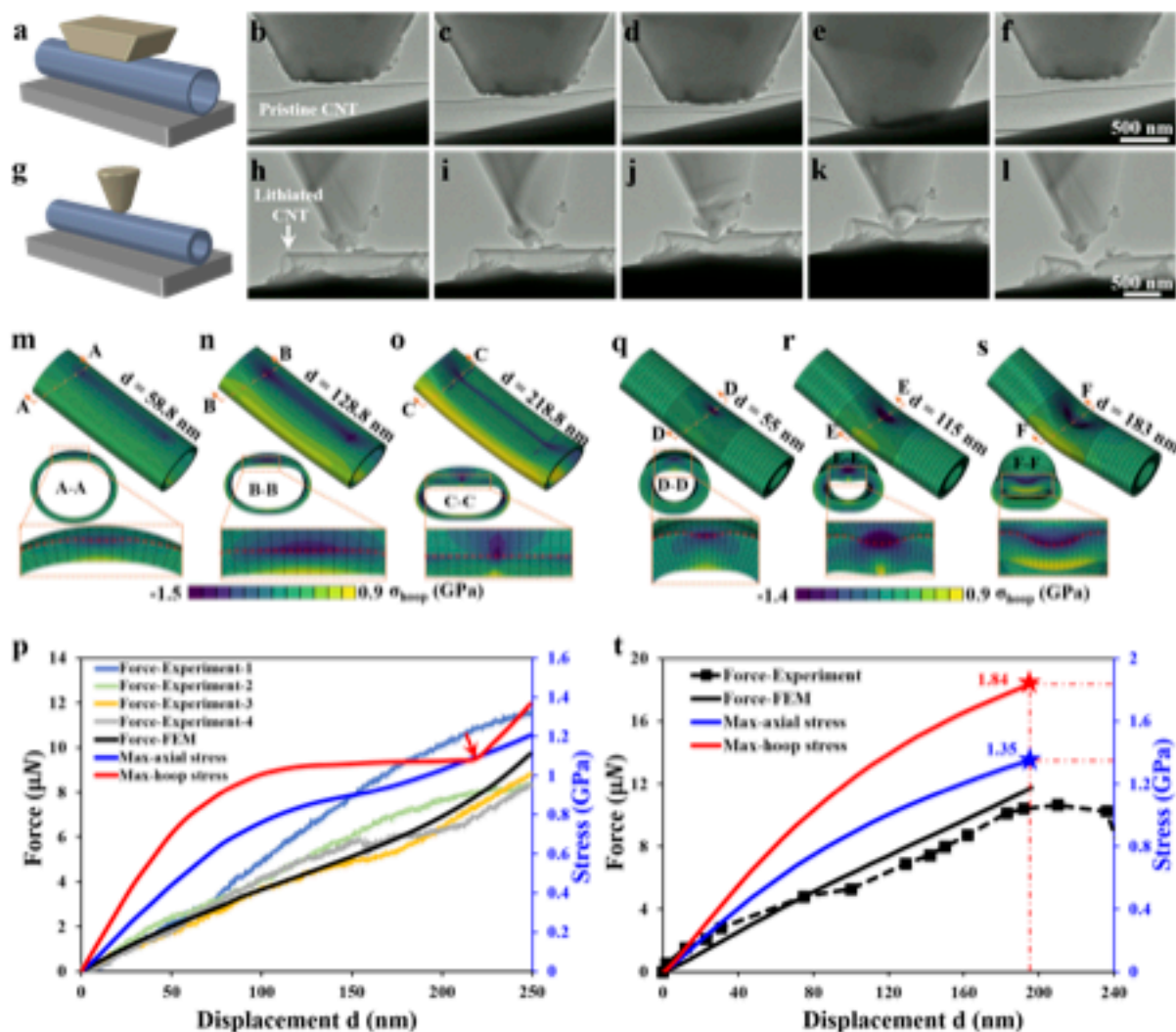


Figure 3. Radial compression of the pristine (a-f, m-p) and lithiated (g-l, q-t) CNTs. (a) and (g) are schematic of the experimental configurations for the compression experiments. (b-f) and (h-l) are sequential TEM images showing the compression processes of the pristine and lithiated CNTs, respectively. Note that for the pristine CNT, it resumed to its initial shape after release of compression (f), indicating good elasticity of the pristine CNT. However, the lithiated CNT exhibits brittle fracture characteristic after compression (l). (m-o) and (q-s) are FEA simulations to the experimental results shown in (b-f) and (h-l), respectively. Both longitudinal and cross-sectional views are provided. (p) and (t) are experimental and simulated force-displacement plots and maximum hoop and axial stress-displacement plots corresponding to (a-f, m-o) and (g-l, q-s), respectively.

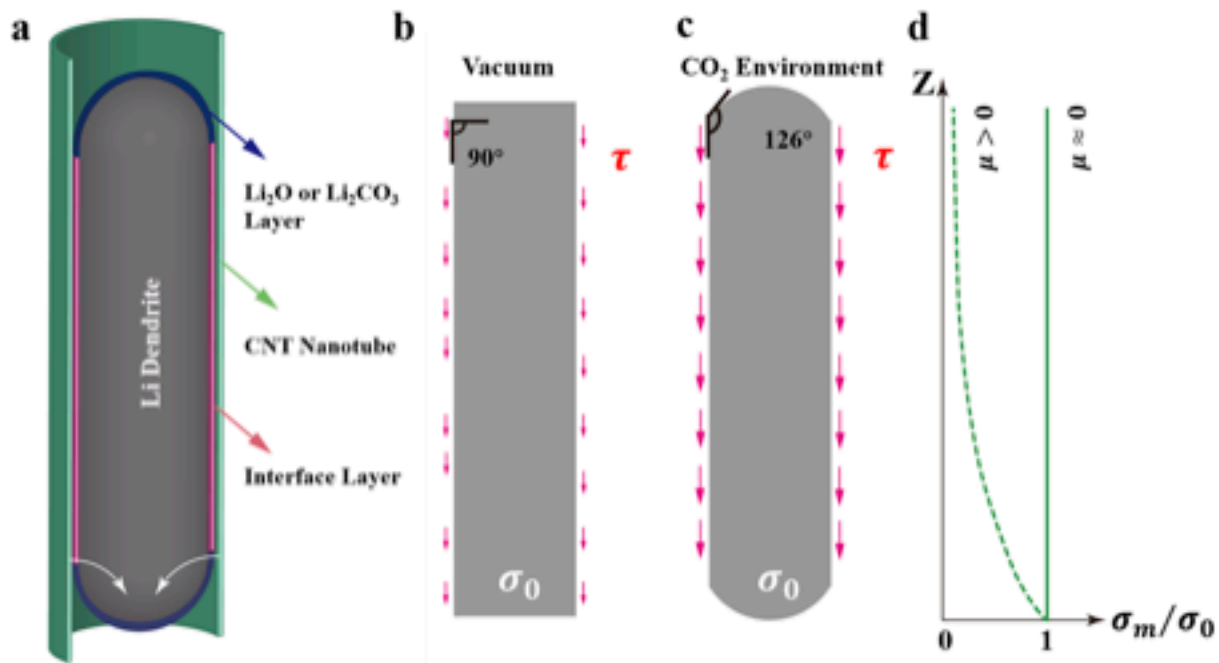


Figure 4. Li deposition dynamics and stress relaxation and accumulation during Li deposition in the CNTs. (a) Schematics of the Li dendrite (Grey) deposited within a CNT (light green). The white arrows point to the deposition site with a deposition stress σ_0 . The deposition stress is transmitted to the Li_2O or Li_2CO_3 layer at the near and far fronts (the light blue). An interface layer, with Li_2CO_3 for the CO_2 TEM environment and Li_2O for vacuum environment, is formed between the Li metal and the lithiated CNT. (b, c) The interfacial shear resistance (τ) scales with the frictional coefficient μ , which depends on the lithiophilicity of the interface. The wetting angles at the interface are $\sim 126^\circ$ in the CO_2 environment and $\sim 90^\circ$ in vacuum, suggesting a smaller μ in vacuum than in the CO_2 environment. (d) Corresponding to the different frictional coefficient, the deposition stress σ_0 may be exponentially decay ($\mu > 0$, for the CO_2 environment) or uniform ($\mu \approx 0$, for the vacuum environment). For the latter the uniform compressive stress propels the propagation of both the Li_2CO_3 layers at the near and far fronts, whereas for the former a symmetry breaking occurs and the near front propagates but the far front arrests.

Table of contents

